Characterization and modeling of non-isothermal crystallization of Polyamide 12 and co-Polypropylene during the SLS process

A. Amado & K. Wegener
Department of Mechanical and Process Engineering, Swiss Institute of Technology, Zürich 8008, Switzerland
M. Schmid & G. Levy
Inspire AG, IRPD Institute for Rapid Product Development, St. Gallen 9014, Switzerland

ABSTRACT: The Selective Laser Sintering (SLS) of thermoplastic materials is actually one of the most promising Additive Manufacturing techniques. The complexity of the process and the interaction between the different phenomena involved has not been fully understood and thus a couple of materials can successfully be processed for production. Empirical evidence indicates that the crystallization behavior has a main influence on the warpage effect, which defines the SLS suitability of a material. The present investigation characterizes and models the non-isothermal crystallization kinetics of a commercial polyamide (PA12) and a new developed polyolefin (coPP) by means of Differential Scanning Calorimetry, integrating the Nakamura model with the Hoffmann-Lauritzen theory. The model results are in good agreement with experiment data below 90% and 65% of relative crystallization for PA12 and coPP respectively. Additionally, a transient FEM simulation of the layer-wise deposition that couples the heat transfer and crystallization kinetics model describes a non-constant stepwise phase change effect per layer related to a sequence of no isothermal and quasi-isothermal states induced by the processing conditions.

1 INTRODUCTION

The Selective Laser Sintering (SLS) is an Additive Manufacturing technology that allows the production of geometrically complex parts in a layer-wise manner, employing basically polymer powders as raw materials. The SLS system consist essentially in a CO_2 laser beam that selectively fuses or melts the polymer particles deposited in a thin layer, which coalesce locally and with the substrate, which corresponds to a previously deposited layer (Gibson et al. 2010). The remaining un-sintered powder acts as a support for the partially fused cross sections until the whole part is completed. Despite the simplicity of the concept, the complexity of the process and the interaction between the different phenomena involved has not been fully understood and only a couple of materials can successfully be processed for production (Schmid & Levy 2009, Drummer et al. 2010, Amado et al. 2011, Rietzel 2011). In this direction, several efforts have been performed to model the process incorporating the different multi-physics involved. The initial model developed by Nelson et al. (1993) employed a one dimensional finite element method to predict the density variations along the vertical build direction for an amorphous thermoplastic (polycarbonate). Ryder et al. (1996) extended the previous model to 2 dimensions, incorporating also the effect of a spatially dependant conductivity and porosity. Papadatos et al. (1997) focused his work in the characterization and the modelling of the bonus-Z phenomenon, by relating it to the energy input. Williams & Deckard (1998) incorporated in their model the sintering law used by Nelson (1993), coupled with the heat transfer and thermal degradation of an amorphous polymer. Bugeda et al. (1999) and Childs et al. (1999) improved the densification model description, including the equations of Mackenzie-Shuttleworth and Scherer for closed and open pore beds. Steinberger et al. (2000) and Schultz (2003) incorporated the viscoelastic effect, a factor that was neglected during the transient coalescence of melted particles. However, Tontowi & Childs (2001a, b) were the first to incorporate a sintering model that considers the latent heat by a temperature recovery method, which takes into account the melting enthalpy of thermoplastics, which are widely used nowadays. More recently different studies have addressed diverse topics such as the volume shrinkage during densification (Dai & Shaw 2005), estimations and measurements of the transient surface temperature during laser scanning (Roberts et al. 2005, Gao et al. 2008, Dong et al. 2009, Xing et al. 2012) and DoE simulations (Sing & Regalla 2010a, b) to obtain high order response surfaces for the sintered density in relation to the laser scanning parameters.

In summary, most of the models found in the literature are focused to simulate the laser beam interaction with the powder bed within a millisecond timeframe, coupling a temperature dependant density function with nonlinear thermal properties. However, none of these models really predicts the processing main difficulties observed when a new polymeric material is tested. Empirical evidence has depicted that among the critical factors, the crystallization behavior has a main influence on the curling or warpage effect, which defines at a first instance the SLS suitability of a powdered material. Drummer et al. (2010) and Rietzel (2011) introduced the concept of crystallization activation energy as an indicator that estimates if a material guarantees certain robustness against under-cooling and thus define the easy of processability for SLS polymers regarding the thermal aspect.

The present study addresses a step further in this direction, characterizing and modeling in more detail the heat transfer coupled to a transient crystallization model by means of Finite Elements Analysis in order to simulate how the polymer phase change develops under SLS processing conditions.

2 THEORETICAL BACKGROUND & EXPERIMENTAL SET UP

2.1 *Crystallization Kinetics Theory*

The overall crystallization kinetics theories describe the evolution of the degree of crystallization $\alpha(t)$ as a function of time t and temperature T. The degree of crystallization is defined as the ratio of the crystallized volume x_C to the ultimate crystallizable volume x_∞ (Boutaous et al. 2010):

$$\alpha(t) = \frac{x_c(t,T)}{x_\infty} \tag{1}$$

For polymer crystallization in quiescent isothermal conditions, the general Avrami equation constitutes the base for the theory developed subsequently for non-isothermal crystallization:

$$\alpha(t) = 1 - \exp(-k(T)t^n) \tag{2}$$

where $k(T)$ is the isothermal crystallization rate constant and n is the Avrami exponent. In a non-isothermal process there is a change of temperature with time, leading to the time dependence of the crystallization rate. For a constant cooling rate, the Ozawa model results from the modification of the Avrami equation (Sajkiewicz et al. 2001):

$$\alpha(t) = 1 - \exp\left(\frac{-\kappa(T)}{|dT/dt|^n}\right) \tag{3}$$

where $\kappa(T)$ is the so called cooling function of non-isothermal crystallization. However, a more general description was developed by Nakamura et al. (1972) for a temperature dependent crystallization rate:

$$\alpha(t) = 1 - \exp\left(-\left(\int_0^t K(T)d\tau\right)^n\right) \tag{4}$$

where $K(T)$ is the non-isothermal crystallization rate. The time differential form of this equation is more useful for modeling, leading to:

$$\frac{\partial\alpha}{\partial t} = nK(T)(1-\alpha)\left[\ln\left(\frac{1}{1-\alpha}\right)\right]^{\frac{n-1}{n}} \tag{5}$$

The Nakamura and Avrami rate constants can be related to each other by the following expression:

$$K(T) = k(T)^{\frac{1}{n}} = \ln(2)^{\frac{1}{n}}\left(\frac{1}{t_{1/2}}\right) \tag{6}$$

where $t_{1/2}$ is the corresponding half crystallization time for a defined isothermal temperature. According to Patel (2011) the determination of the reciprocal half crystallization time can be expressed by the Hoffman-Lauritzen theory:

$$\left(\frac{1}{t_{1/2}}\right) = K_0 \exp\left(\frac{-U}{R(T-T_\infty)}\right)\exp\left(\frac{-K_G(T+T_o)}{2T^2\Delta T}\right) \tag{7}$$

where K_0 is a temperature independent constant, U is the activation energy of the crystallization transport which takes the universal value of 6270 J/mol, R is the universal gas constant equal to 8.314 J/mol/K and $T_\infty = T_G - 30°K$ is the temperature at which the crystallization transport finishes, with T_G the related glass transition temperature. K_G is related to the nucleation characteristics and $\Delta T = T_o - T$ corresponds to the under-cooling from the equilibrium melting point T_o, which can be determined by the Hoffman-Weeks construction (Patel & Spruiell 1991). To determine K_0 and K_G different isothermal measurements need to be performed by means of differential scanning calorimetry (DSC).

2.2 *Heat Transfer Model*

The equation that governs the heat transfer process of the SLS powder bed inside the build cylinder during the cooling stage is defined as follows:

$$\rho_{eff}(\alpha,T)Cp_{eff}(\alpha,T)\frac{\partial T}{\partial t} = \nabla\cdot\left(k_{eff}(\alpha,T)\cdot\nabla T\right) + Q \tag{8}$$

$$Q = \begin{cases} \rho_{eff}(\alpha,T)\Delta H_c\dfrac{\partial\alpha}{\partial t} & \text{for melted regions} \\ 0 & \text{for unsintered powder} \end{cases} \tag{9}$$

where $\rho_{eff}(\alpha,T)$ corresponds to the effective density, $Cp_{eff}(\alpha,T)$ to the effective heat capacity and $k_{eff}(\alpha,T)$ to the effective thermal conductivity. ΔH_c accounts for the crystallization enthalpy. The crystallization rate was previously defined in Equation 5. The material properties are also defined as a function of the relative crystallinity during the phase change and expressed by the following relations:

$$\begin{aligned} \rho(\alpha,T) &= \alpha\rho_s(T) + (1-\alpha)\rho_m(T) \\ Cp(\alpha,T) &= \alpha Cp_s(T) + (1-\alpha)Cp_m(T) \\ k(\alpha,T) &= \alpha k_s(T) + (1-\alpha)k_m(T) \end{aligned} \quad (10)$$

where the subscripts s and m denote the solid and melted states respectively of the bulk material. Then, according to Steinberger et al. (2000), the effective material properties can be defined by:

$$\begin{aligned} \rho_{eff}(\alpha,T) &= x_{rel}\rho(\alpha,T) \\ Cp_{eff}(\alpha,T) &= x_{rel}Cp(\alpha,T) + (1-x_{rel})Cp_{N2} \\ k_{eff}(\alpha,T) &= x_{rel}k(\alpha,T) + (1-x_{rel})k_{N2} \end{aligned} \quad (11)$$

where Cp_{N2} and k_{N2} are the heat capacity and thermal conductivity of the chamber atmosphere (95% N_2). x_{rel} accounts for the material fraction which is defined for each domain as follows:

$$x_{rel} = \begin{cases} x_{rel.\,parts} & \text{for melted regions} \\ x_{rel.\,powder\,bed} & \text{for unsintered powder} \end{cases} \quad (12)$$

2.3 *Materials & Experimental Set Up*

For this study two commercial SLS thermoplastic polymers were considered, namely DuraformPA® (3DSystems, USA) and icoPP (Inspire IRPD, Switzerland). The first corresponds to a polyamide 12 (PA12) and the second to a co-polypropylene. A standard thermal characterization by means of DSC at a heating/cooling rate of 10°C/min is depicted in Figure 1. The thermal properties and densities for both materials are summarized in Table 1. The heat capacity was measured by DSC employing Al_20_3 as a reference for the range between 30°C and 290°C. For PA12, the density or specific volume and the thermal conductivity were reported by Rietzel et al. (2011) and Yuan et al. (2011) respectively. In case of the co-polypropylene, these properties were estimated from the literature (Ehrenstein et al. 2004, Osswald & Hernández-Ortiz 2006, Zhang et al. 2002). For nitrogen, the data reported by Bergman et al. (2011) was used.

For each material, a set of 6 isothermal and 6 non-isothermal measurements were performed using a Mettler DSC 30 previously calibrated with indium. Samples of 5 mg and 15 mg were prepared in 40 µl aluminum pans for PA12 and icoPP respectively.

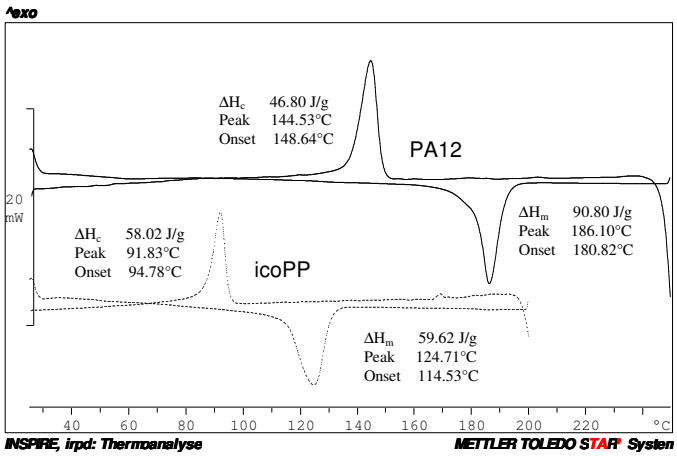

Figure 1. DSC results for PA12 & icoPP (10°C/min).

Table 1. Thermal properties & density of bulk PA12 and icoPP (T in [°C]).

Property	PA12	icoPP
ρ_s [kg/m^3]	1010-0.688T	885-0.315T*
ρ_m [kg/m^3]	961-0.6162T	836-0.334T*
Cp_s [J/kg/K]	1399+9.1e-3T	1398+1.3e-2T
Cp_m [J/kg/K]	1928+3.6e-3T	1914+3.8e-3T
k_s [W/m/K]	0.28-2.5e-4T	0.23-2e-4T*
k_m [W/m/K]	0.24-1e-5T	0.16-8e-5T*
ΔH_m [J/g]**	90.8	59.6
ΔH_c [J/g]**	46.8	58.0
T_G [°C]	51	-10*
$x_{rel.\,parts}$ [%]	97	98
$x_{rel.\,powder\,bed}$ [%]	42	55
	N_2 (at 420K)	
k_{N2} [W/m/K]	0.033*	
Cp_{N2} [J/kg/K]	1049*	

* Data estimated from literature. ** Measured at 10°C/min

The measurements were carried out under dry nitrogen gas. For both test, the sample temperature cycle consisted of an initial constant heating rate of 20°C/min from room temperature (T_i=25°C) to the temperature set for the powder bed top surface (T_s) under SLS operation. These values are 172°C and 117°C for PA12 and icoPP respectively. This temperature was held for 2 min, followed by a heating rate of 40°C/min until a ΔT of 50°C is achieved. Afterwards, a cooling rate of 40°C/min was set until a constant temperature T_{iso} is reached (isothermal case) or before a lower defined cooling rate R begins (non-isothermal case). For the isothermal experiments, 6 different temperatures were considered, starting from 172°C to 166°C with a ΔT of 1°C. For the non-isothermal tests, after reaching the part bed temperature, 6 different cooling rates were defined, starting from 0.1°C/min to 3.2 C/min following a geometrical progression. After each sample fully crystallizes, a reheating was performed at 20°C/min until the polymer was completely melted again. This last step was performed to estimate the equilibrium melting point T_o by the Hoffman-Weeks construction. A graphical representation of the temperature sequence described is depicted in Figures 3 and 9.

3 TRANSIENT FINITE ELEMENT SIMULATION

3.1 *FEM Model Layout*

A SLS system consist of a central build platform were the powder is deposited layer by layer, with a laser beam scanning stage in-between. The aim of this investigation is to simulate how the materials relative crystallization develops when a geometrical simple part (thin disk) is built. For this purpose the software COMSOL® v4.2 is used. The geometry of a 3DSystem SLS 2000 powder bed is considered. Due to the axial symmetry of the powder bed a 2D axisymmetric FEM model is defined as depicted in Figure 2. The disk is located at the center of the powder bed (diameter 2*D*) with a radius *r* and height *h*. During processing, the top of the powder bed is held at a temperature T_s, while the lateral sides and bottom remain at a lower temperature T_b. At the beginning of the simulation, only the powder bed with a height *B* is considered. Afterwards, a new layer of thickness *t* is added, with an initial temperature T_f. This layer is divided in two regions: a cross section of the sintered disk and the un-sintered powder. As the energy supplied by the laser allows the coalescence of the powder and an overheating of the material, the surface temperature of the disk increases above T_s. However, the time delay between successive powder recoating cycles allows the temperature to drop until T_s is reached. For this reason the effect of the laser in not taken into account directly. Instead, after laser scanning the sintered region remains in a meta-stable state, were the crystallization enthalpy has still not been released. Afterwards, the cycle is repeated until the part is completed.

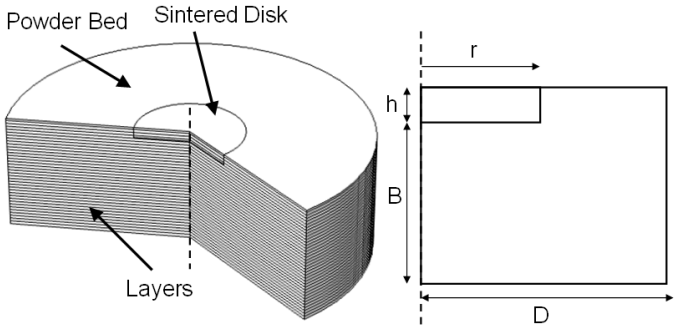

Figure 2. Powder bed cylinder geometry.

3.2 *Boundary Conditions & Assumptions*

The initial and boundary conditions for a standard build with each material are summarized in Table 2. Regarding the geometrical dimensions, the following values were employed: *r*=50mm, *h*=1mm and *D*=165mm. Additionally, the following assumptions have been made:

- The contact between sintered layers and between layers and powder bed is perfect.
- The transient powder coalescence (shrinkage) has been neglected (constant layer thickness).
- Each new layer added is assumed to be deposited instantly over the whole surface.
- The effective density of the parts and the powder bed are assumed to remain constant for each domain. These values were previously measured from sintered parts and small sintered boxes with powder inside (see Table 1).
- The surface temperature T_s is considered as a transient boundary condition measured by the infrared sensors of the SLS machine.

Table 2. Initial & boundary conditions for PA12 and icoPP.

Parameter	PA12	icoPP
T_{s0}[°C]	172	117
T_b [°C]	130	95
T_f [°C]	130	70
t [µm]	100	100
B [mm]	15	15
$t_{layer\ delay}$ [s]	40	40

Inspire irpd, Switzerland.

4 RESULTS & ANALYSIS

4.1 *Isothermal Measurements*

The results obtained for the isothermal measurements are depicted in Figures 3 and 6. For both materials it can be observed that as the isothermal temperature is reduced, the time at which the signal reaches a maximum is considerable lowered. The results for the calculated half crystallization time are presented in Table 2. It must be pointed out that for icoPP, the maximum isothermal temperature at which an adequate heat flow signal could be obtained was 111°C, which is 5°C below the temperature at which the powder bed is held (117°C). This can be explained due to the lower difference with the onset/peak melting temperature, hindering crystallization.

Table 3. Isothermal half crystallization times.

PA12					
T [°C]	166	167	168	169	170
$t_{1/2}$ [min]	15.9	22.0	32.4	57.9	103.3
icoPP					
T [°C]	106	107	108	109	110
$t_{1/2}$ [min]	16.1	23.5	34.1	49.3	72.5

Table 4. Isothermal Avrami exponent and rate constant.

PA12			icoPP		
T [°C]	n [/]	k [1/s^n]*e9	T [°C]	n [/]	k [1/s^n]*e8
166	2.80	3.162	106	2.40	8.248
167	2.77	1.580	107	2.40	3.664
168	2.57	2.489	108	2.45	0.627
169	2.53	0.744	109	2.40	0.351
170	2.42	0.444	110	2.44	0.132

In case of PA12, 171°C was the maximum temperature at which a signal was obtained. With this data a double logarithmic representation was used to analyze if the crystallization behavior follows the Avrami model. In Figures 4 and 7 it can be observed how PA12 presents a more linearized behavior during the whole crystallization range and for the different temperatures in comparison to icoPP. Also a linear fit was performed and the Avrami constants are presented in Table 4. According to the literature,

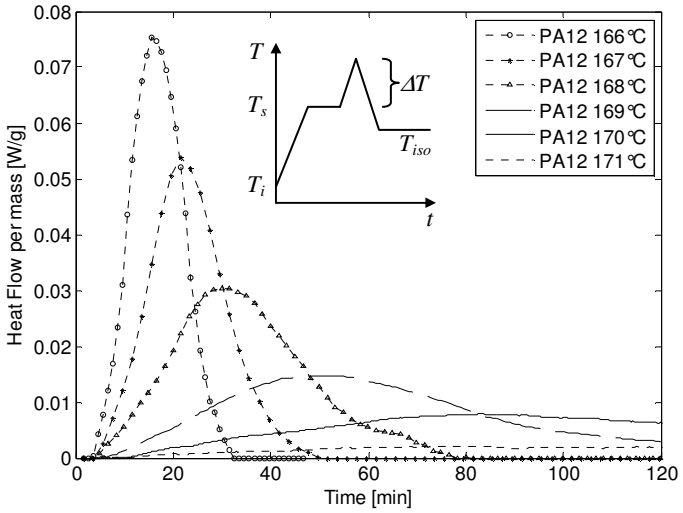

Figure 3. Isothermal curves for PA12 at different temperatures.

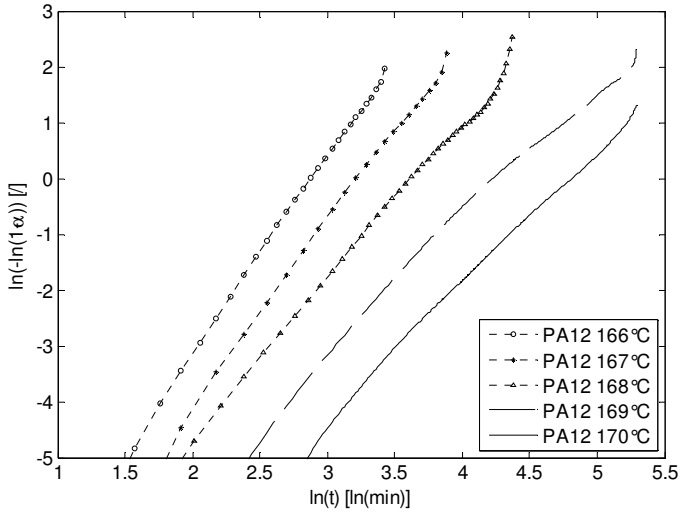

Figure 4. Logarithmic representation of isothermal curves for PA12 at different temperatures.

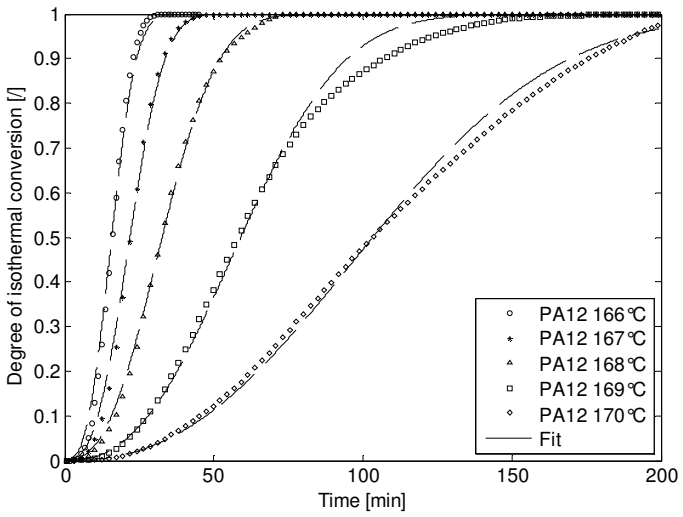

Figure 5. Fitted curves with Avrami parameters for the degree of isothermal conversion for PA12 at different temperatures.

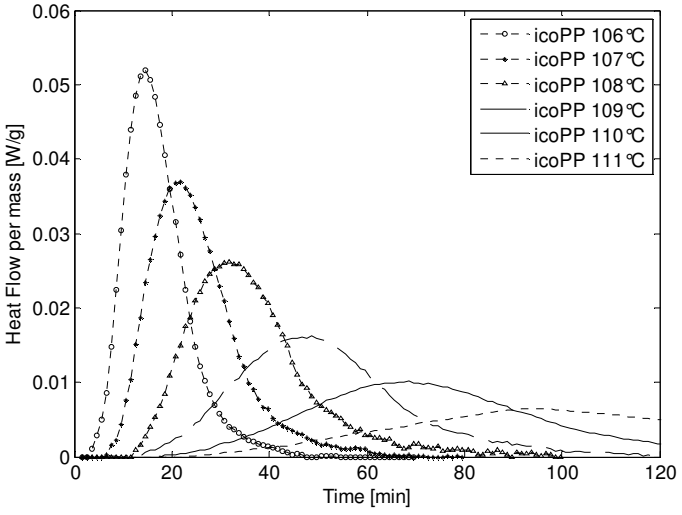

Figure 6. Isothermal curves for icoPP at different temperatures.

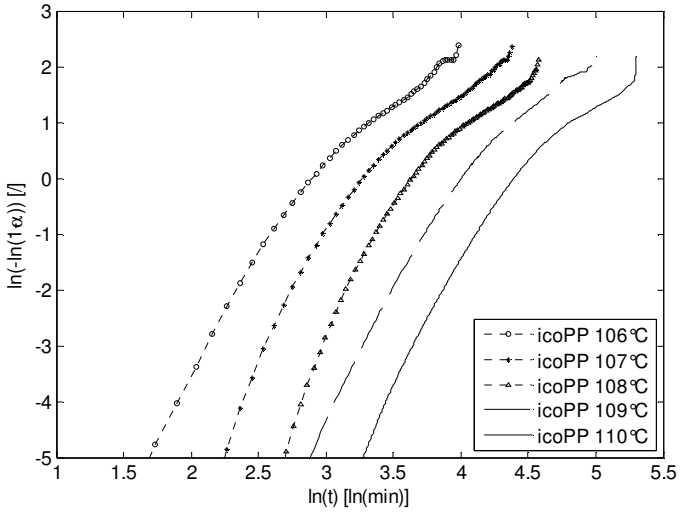

Figure 7. Logarithmic representation of isothermal curves for icoPP at different temperatures.

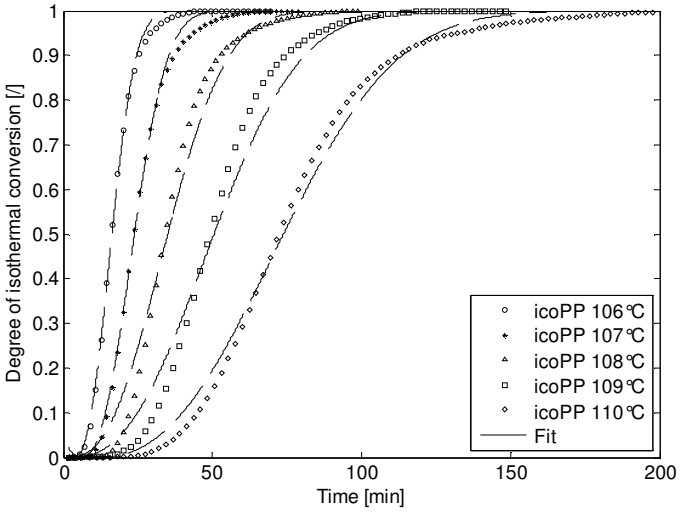

Figure 8. Fitted curves with Avrami parameters for the degree of isothermal conversion for icoPP at different temperatures.

a direct interpretation of both constants in not so clear, particularly the value of the Avrami exponent *n*, which is related to the structure of the crystal and its nature of nucleation while the constant *k* is related to the speed of crystallization (Yang et al. 2005). In case of PA12, as the isothermal temperature is reduced, the exponent approaches the value of 3, which is theoretically related to a spherical growth of homogenously nucleated spherulites with instant nucleation. In case of icoPP, the exponent remains constant at a value of 2.4, related to more flattened structures (plane growth) with sporadic nucleation. Figures 5 and 8 depict the curves fitted with these parameters for the different temperatures. As observed, PA12 can clearly be characterized by the Avrami theory. In case of icoPP the model can be suitable for a degree of isothermal conversion between 20% and 80%, particularly for higher values of under-cooling. However, it is out of the scope of this work to discuss further the physical validity of the Avrami theory.

4.2 *Non-Isothermal Measurements*

The results for the non-isothermal measurements are depicted in Figures 9 and 11. It can be observed that as the cooling rates decrease, the crystallization of both materials begins at a higher temperature, reducing the effective temperature window for SLS processing in comparison to standard DSC measurements at 10°C/min. The half crystallization times for the different cooling rates and materials are depicted in Table 5. It is important to note that, for similar cooling rates, icoPP presents higher values for $t_{1/2}$.

Table 5. Non-isothermal half crystallization times.

PA12						
R[°C/min]	0.1	0.2	0.4	0.8	1.6	3.2
$t_{1/2}$ [min]	66.9	38.4	24.4	14.7	9.1	5.5
icoPP						
R[°C/min]	0.1	0.2	0.4	0.8	1.6	3.2
$t_{1/2}$ [min]	104.5	65.5	39.0	22.1	12.4	6.9

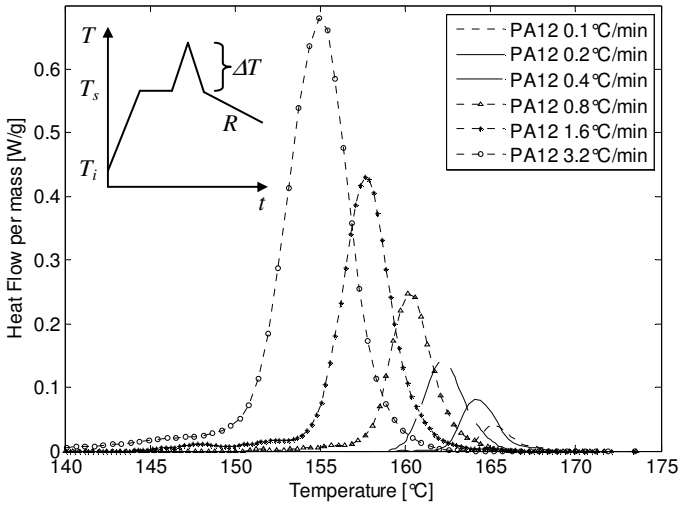

Figure 9. Non-isothermal curves for PA12 at different cooling rates.

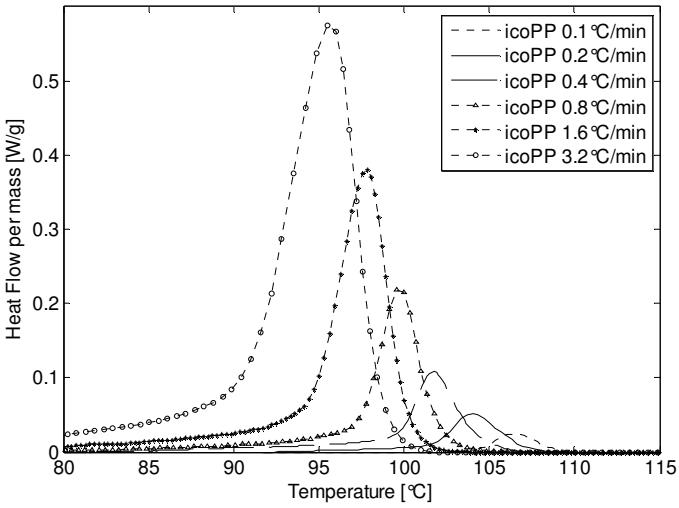

Figure 11. Non-isothermal curves for icoPP at different cooling rates.

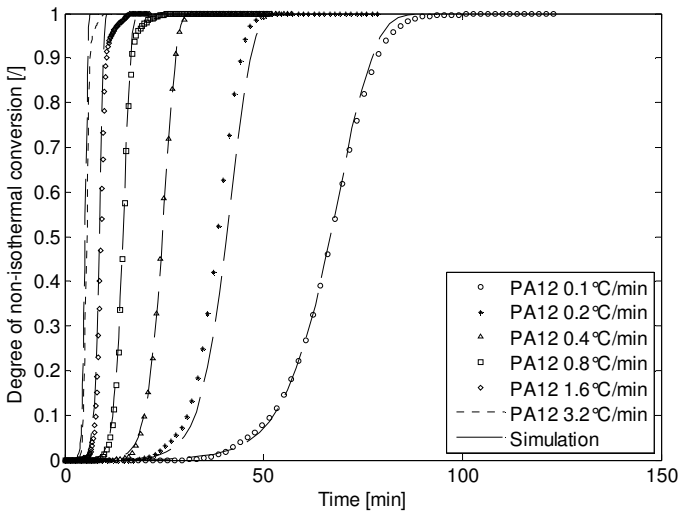

Figure 10. Simulated curves for the degree of non-isothermal conversion for PA12 at different cooling rates.

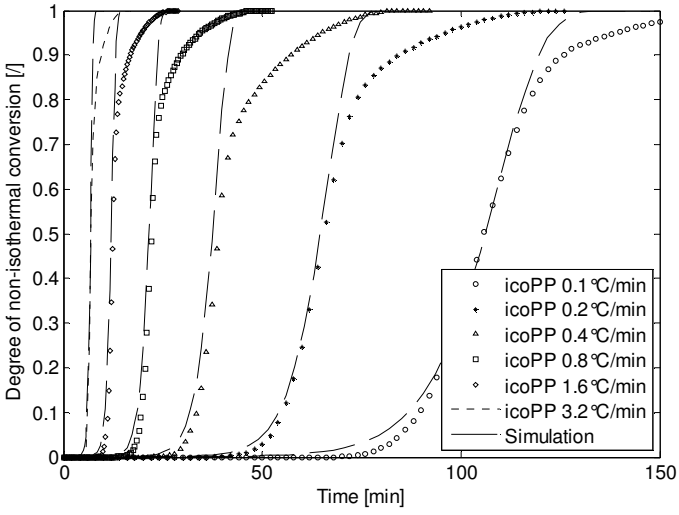

Figure 12. Simulated curves for the degree of non-isothermal conversion for icoPP at different cooling rates.

Table 6. Hoffman-Lauritzen calculated parameters.

Parameter	PA12	icoPP
K_o [1/s]	5.560e4	3.924e10
K_G [K^2]	140,866	498,964
T_o [°C]	192.4	160
T_∞ [°C]	21	-40

This is explained due to the particular measurement conditions, were the starting temperature for icoPP is closer to the melting peak temperature related to the powder bed temperature used for SLS processing. With the measurements of $t_{1/2}$ for the isothermal case, the values of K_0 and K_G of Equation 7 can be obtained by a linear least square fitting. These parameters do not present a direct physical interpretation, but K_G is related to the nucleation characteristics associated to the mode of nucleation, thickness of the growth layers (lamellas) and their lateral surface energies (Reiter & Sommer 2003). The equilibrium melting temperature T_0 can be estimated by representing the melting temperature of the isothermally crystallized samples in terms of the isothermal temperature employed for crystallization T_c and find the cutoff line with the graphic T_m vs. T_c (Hoffman-Weeks construction). All the values obtained are summarized in Table 6. Finally, to validate the suitability of the Nakamura model coupled with the Hoffman-Lauritzen theory, Equations 5 to 7 were solved numerically with COMSOL®, simulating the non-isothermal crystallization experiments for both polymers at the different cooling rates, using an average value of the Avrami constant n for both materials. Thus, for PA12, the model fits quite well the experimental results, at least below 90% of the total conversion (Figure 10). In case of icoPP, the fit results suitable below 65% (Figure 12). Above this value, the model over predicts the experimental results. These differences can be attributed to other crystallization mechanisms, such as transcrystallinity effects due to the contact with the DSC pan and the final impingement of bulk nucleated spherulites (Billon et al. 1994, Cunha & Fakirov 2000).

4.3 *Temperature Measurements & Simulation*

The FEM model consists of a 2D mesh with 10,360 quadrilateral second order elements (85,030 dof). The crystallization expression was coupled with the heat transfer equation using the distributed ordinary differential equation interface of COMSOL®. The time step employed was fixed at 0.1s using a sequential step solver. The first 10 deposited layers were considered for the current analysis. Figure 13 depicts the temperature distribution of the powder bed using icoPP. As observed, the steepest temperature gradient is present along the build orientation z. Thus the crystallization effect was analyzed along

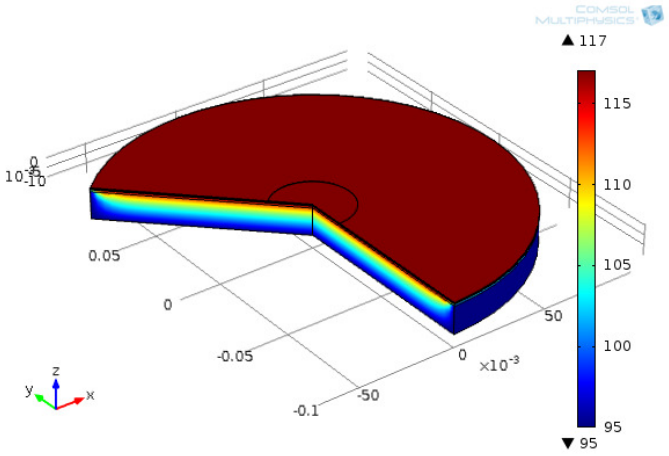

Figure 13. Temperature distribution of icoPP powder bed.

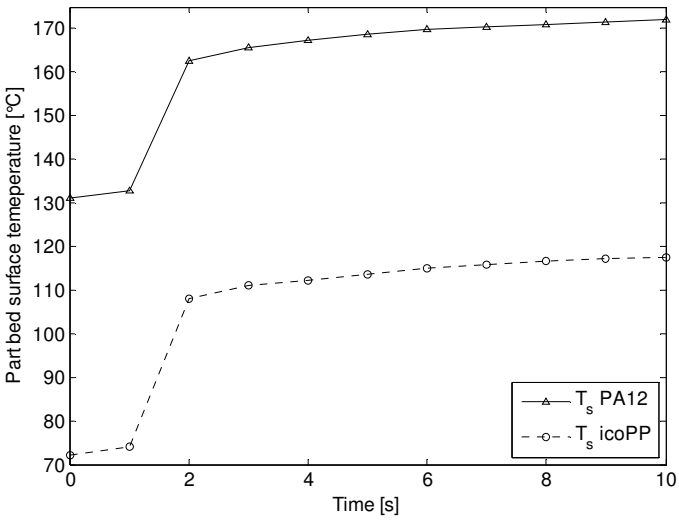

Figure 14. Measured *Ts* evolution on the SLS powder bed surface for PA12 & icoPP.

this direction. Regarding the boundary condition of the top powder bed surface, the cyclic evolution of the temperature T_s was obtained from the measurements taken on the powder bed by the chamber infrared sensor. Figure 14 depicts the results for PA12 and icoPP (average values from 5 cycles). Employing this data, the simulation begins with the deposition of powder over the first melted layer (L1). After the initial temperature drop corresponding to the addition of a new layer preheated at a temperature T_f (see Table 2), the powder is heated again to reach the defined powder bed temperature. During the following holding time, the powder is melted by the laser, generating also an overheating of the layer. However, this temperature increase is neglected due to the considerable high holding time that allows the material to recover the initial temperature. Afterwards, a new layer is added and the sequence is repeated. Figures 15 and 17 depict the paths of the simulated temperature variation at the middle point of each layer. As noted, as a new layer is added, the layer below reduces its temperature. In case of PA12, after approximately 7 minutes, the first layer

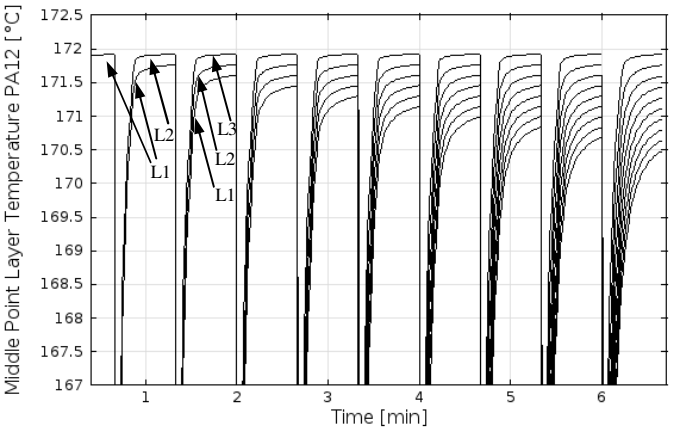

Figure 15. Temperature at the middle point of each layer (PA12).

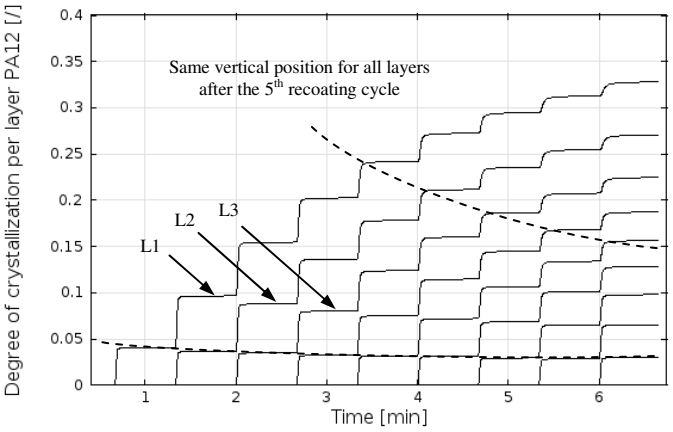

Figure 16. Cumulative degree of crystallization for each layer (PA12).

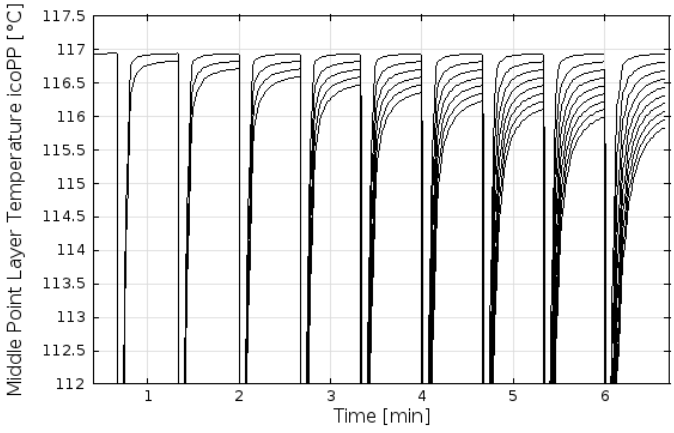

Figure 17. Temperature at the middle point of each layer (icoPP).

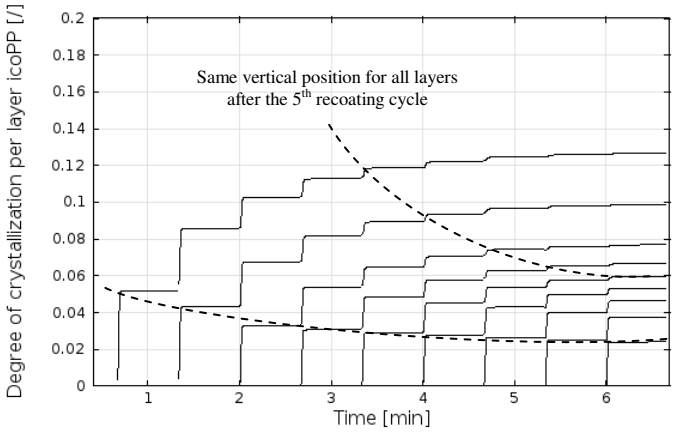

Figure 18. Cumulative degree of crystallization for each layer (icoPP).

presents an average reduction of approximately 1.5°C which corresponds to an average cooling rate of 0.23°C/min. In case of icoPP, this variation is lower with a value of 1.2°C and a corresponding cooling rate of 0.18°C/min. This difference is closely related to the particular production conditions employed for each material. However, it is important to note that PA12 experiences an average cooling rate 28% higher. Figure 16 and 18 depict the cumulative degree of crystallization for each layer and each material. An interesting "stairs-pattern" can be observed for each layer which can be described as a non-constant stepwise crystallization effect. This pattern consist of two elements: a steep crystallization change induced by the fresh powder added with each new layer and a relative constant crystallized state during the holding period in-between. This steep crystallization change is higher for the first layers and reduces continuously as the height of the build progresses. In case of PA12, after 5 recoating cycles, the first layer presents a 24% degree of crystallization and achieves a value of 33% until the tenth layer has been deposited. In case of icoPP, after 5 recoating cycles, the first layer presents a 12% degree of crystallization and remains almost constant for the subsequent deposited layers.

This constant value indicates that the under-cooling effect of each new layer added has no further influence on the crystallization behavior below this vertical position. Moreover, for both materials an interesting effect is observed as the degree of conversion increases: for a same build position below the powder bed surface, the layers do not present the same degree of crystallization. This trend is depicted in Figure 16 and 18 were the first layer presents a higher conversion in comparison to the fifth (depicted by a dotted line). This behavior can be related to the partial release of the total enthalpy of crystallization, i.e., to the fraction of total phase change energy that is released. Thus, as the first layers crystallize, there is a continuous transfer of energy to the subsequent layers, slightly increasing the temperature. This counteracts the under-cooling effect and hinders crystallization. It must be also pointed out that for icoPP, despite the inaccuracies of the Nakamura model with the experimental results due to the over-prediction of the crystallization kinetics, the results can be used with confidence while a conversion degree above 65% is not reached.

As a final comment, neglecting the effect of the laser directly can induce also some distortions, particularly for the first two layers, since the higher temperature induced by the laser can erase the formation of

nuclei from the layers below. However, due to the low penetration depth at the wavelength of CO_2 lasers in thermoplastics as reported by different authors (Steinberger et al. 2000, Klein 2011), for the materials employed this variable does not exceed a value of 200 µm (~2 layers). Thus, the crystallization curves will not be affected from the second recoating cycle and will develop a similar trend that presented in this work.

5 SUMMARY

An isothermal and non-isothermal characterization was performed for DuraformPA® and icoPP, two commercial SLS powders. The crystallization modeling of both polymers by integrating the Nakamura model with the Hoffmann-Lauritzen theory for the determination of the crystallization rate constant demonstrates to be in very good agreement with experimental results for PA12. In case of icoPP, the model results suitable below the 65% of crystallinity. With these results, a transient FEM simulation was performed for the first 10 deposited layers during a normal SLS build. As a main result, a "stairs-pattern" effect was observed for each layer, which can be described as a non-constant stepwise crystallization, corresponding to a sequence of no isothermal and quasi-isothermal states. According to the particular processing condition used for each material, after 10 deposited layers, PA12 and icoPP present a maximum crystallization degree of 33% and 12% respectively. As future work, a detailed analysis of the laser effect will be considered. Additionally, coupling the themo-mechanical properties with these crystallization results is proposed in order to obtain a better understanding how the warpage or curling of parts develops during a SLS build and thus validate the simulation results obtained.

6 ACKNOWLEDGMENTS

The authors would like to thank the European Seventh Framework Programme for the financial support provided through the "Step Up" project (Grant Agreement Number NMP2-SE-2008-213927).

7 REFERENCES

Amado, A., Schmid, M., Levy, G. & Wegener, K. 2011. Advances in SLS Powder Characterization. *Proceedings of the Solid Freeform Fabrication Symposium*, Austin, TX, pp. 438-452.

Bergman, T.L., Lavine, A.S., Incropera, F.P. & DeWitt, D.P. (7th ed.) 2011. Fundamentals of Heat and Mass Transfer. New York: John Wiley & Sons.

Billon, N., Magnet, C., Haudin, J. M. & Lefebvre, D. 1994. Transcrystallinity effects in thin polymer films. Experimental and theoretical approach. *Colloid & Polymer Science* 272(6): 633-654.

Boutaous, M., Brahmia, N. & Bourgin, P. 2010. Parametric study of the crystallization kinetics of a semi-crystalline polymer during cooling. *Comptes Rendus Mécanique* 338(2): 78-84

Bugeda, G., Cervera, M. & Lombera, G. 1999. Numerical prediction of temperature and density distributions in selective laser sintering processes. *Rapid Prototyping Journal* 5(1): 21-26.

Cunha, A.M. & Fakirov, S. 2000. Structure Development During Polymer Processing. *Proceedings of the NATO Advanced Study Institute on Structure Development in Processing for Polymer Property Enhancement*. E 370: 133-136.

Childs, T.H.C., Berzins, M., Ryder, G.R. & Tontowi, A.E. 1999. Selective laser sintering of an amorphous polymer-simulations and experiments. *Proceeding of the Institution of Mechanical Engineers. Part B* 213(4): 333–349.

Dai, K. & Shaw, L. 2005. Finite element analysis of the effect of volume shrinkage during laser densification. *Acta Materialia* 53(18): 4743-4754.

Dong, L., Makradi, A., Ahzi, S. & Remond, Y. 2009. Three-dimensional transient finite element analysis of the selective laser sintering process. *Journal of Materials Processing Technology* 209(2): 700–706.

Drummer, D., Rietzel, D. & Kühnlein, F. 2010. Development of a characterization approach for the sintering behaviour of new thermoplastics for selective laser sintering. *Physics Procedia: Proceedings of the LANE*. Part B 5: 533-542.

Ehrenstein, G., Riedel, G. & Trawiel, P. (1st ed.) 2004. *Thermal Analysis of Plastics: Theory and Practice*. Munich: Hanser.

Gao, Y., Xing, J., Zhang, J., Luo, N. & Zheng, H. 2008. Research on measurement method of selective laser sintering (SLS) transient temperature. *Optik - International Journal for Light and Electron Optics* 119(13): 618-623.

Gibson, I., Rosen, D. W. & Stucker, B. (1st ed.) 2010. *Additive Manufacturing Technologies Rapid Prototyping to Direct Digital Manufacturing*. New York: Springer.

Klein, R. (1st ed.) 2011. *Laser Welding of Plastics*. Berlin: Wiley-VCH.

Nakamura, K., Watanabe, T., Katayama, K. & Amano, T. 1972. Some aspects of nonisothermal crystallization of polymers. I. Relationship between crystallization temperature, crystallinity, and cooling conditions. *Journal of Applied Polymer Science* 16(5): 1077-1091.

Nelson, J.C. 1993. Selective Laser Sintering: a definition of the process and the empirical sintering law. *PhD Dissertation, The University of Texas at Austin*, Austin, TX, USA.

Nelson, J.C., Xue, S., Barlow, J.W., Beaman, J.J., Marcus, H.L. & Bourell, D.L. 1993. Model of the selective laser sintering of Bisphenol-A polycarbonate. *Industrial & Engineering Chemistry Research* 32(10): 2305–2317.

Osswald, T.A. & Hernández-Ortiz, J.P. (1st ed.) 2006. *Polymer Processing: Modeling and Simulation*. Munich: Hanser.

Papadatos, A., Ahzi, S., Deckard, C. & Paul, F. 1997. On dimensional stability: modelling the Bonus-Z during the SLS process. *Proceedings of the Solid Freeform Fabrication Symposium*, Austin, TX, pp. 709-716.

Patel, R.M. & Spruiell, J.E. 1991. Crystallization kinetics during polymer processing - Analysis of available approaches for process modeling. *Polymer Engineering & Science* 31(10): 730-738

Patel, R.M. 2011. Crystallization kinetics modeling of high density and linear low density polyethylene resins. *Journal of Applied Polymer Science* 124(2): 1542-1552

Reiter, G & Sommer, J.U. (1st ed.) 2003. *Polymer Crystallization: Observations, Concepts and Interpretations (Lecture Notes in Physics)*. Berlin: Springer.

Rietzel, D., Drexler, M., Kühnlein, F. & Drummer, D. 2011. Influence of temperature fields on the processing of polymer powders by means of laser and mask sintering technology. *Proceedings of the Solid Freeform Fabrication Symposium*, Austin, TX, pp. 252-262.

Rietzel, D. 2011. Werkstoffverhalten und Prozessanalyse beim Laser-Sintern von Thermoplasten. *PhD Dissertation, Technischen Fakultät der Universität Erlangen-Nürnberg*, Erlangen , Germany.

Roberts, I.A, Wang, C.J., Esterlein, R., Stanford, M. & Mynors, D.J. 2005. A three-dimensional finite element analysis of the temperature field during laser melting of metal powders in additive layer manufacturing. *International Journal of Machine Tools & Manufacture* 49(12-13): 916-923.

Ryder, G. J., Berzins, M. & Childs, T.H.C. 1996. Modelling Simple Feature Creation in Selective Laser Sintering. *Proceedings of the Solid Freeform Fabrication Symposium*, Austin, TX, pp. 567-574.

Sajkiewicz, P., Carpaneto, L. & Wasiak, A. 2001. Application of the Ozawa model to non-isothermal crystallization of poly(ethylene terephthalate). *Polymer* 42(12): 5365-5370.

Schmid, M. & Levy, G. 2009. Lasersintermaterialien - aktueller Stand und Entwicklungspotential. *Fachtagung Additive Fertigung*, Lehrstuhl für Kunststofftechnik, Erlangen, Germany, pp. 43-55.

Schmid, M., Amado, F. & Levy, G. 2011. iCoPP- A New Polyolefin for Additive Manufacturing (SLS). *Proceedings of the International Conference on Additive Manufacturing*, Loughborough, UK.

Schultz, J.P. 2003. Modeling Heat Transfer and Densification during Laser Sintering of Viscoelastic Polymers, *PhD Dissertation, Virginia Polytechnic Institute and State University*, Blacksburg , VA, USA.

Singh, A.K., Regalla S.P. 2010a. Response surface-based simulation modeling for selective laser sintering process. *Rapid Prototyping Journal* 16(6): 441-449.

Singh, A.K., Regalla S.P. 2010b. DOE based three-dimensional finite element analysis for predicting density of a laser-sintered part. *Rapid Prototyping Journal* 16(6): 460-467.

Steinberger, J., Shen, J., Manetsberger, K. & Muellers, J. 2000. The Simulation of the SLS Process as the Basis of a Process Optimization. *Proceedings of the Solid Freeform Fabrication Symposium*, Austin, TX, pp. 377-385.

Tontowi, A.E. & Childs, T.H.C 2001a. Density prediction of crystalline polymer sintered parts at various powder bed temperatures. *Rapid Prototyping Journal* 7(3): 180-184.

Tontowi, A.E. & Childs, T.H.C 2001b. Selective laser sintering of a crystalline and a glass-filled crystalline polymer: Experiments and simulations. *Proceeding of the Institution of Mechanical Engineers. Part B* 215(11): 1481–1495.

Williams J.D. & Deckard, C.R. 1998. Advances in modeling the effects of selected parameters on the SLS process. *Rapid Prototyping Journal* 4(2): 90-100.

Xing, J., Sun, W. & Rana, R.S. 2012. 3D modeling and testing of transient temperature in selective laser sintering (SLS) process. *Optik - International Journal for Light and Electron Optics*, in press.

Yang, J., McCoy, B.J. & Madras, G. 2005. Distribution kinetics of polymer crystallization and the Avrami equation. *Journal of Chemical Physics* 122(6): 064901.

Yuan, M., Bourell, D. & Diller, T. 2011. Thermal Conductivity Measurements of Polyamide 12. *Proceedings of the Solid Freeform Fabrication Symposium*, Austin, TX, pp. 427-437.

Zhang, X., Hendro, W., Fuji, M., Tomimuta, T. & Imaishi, N. 2002.Measurements of the Thermal Conductivity and Thermal Diffusivity of Polymer Melts with the Short-Hot-Wire Method. *International Journal of Thermophysics* 23(4): 1077-1090